Analytical and Computational Study of Nonplanar Wings

Independent Project

Jaswin Hargun, Nachat Jatusripitak, Irura Nyiha

Dr. Mika Latva-Kokko

Spring 2020

Abstract

Nonplanar wings have been a point of interest in aerodynamics research, promising reduced induced drag while maintaining the same wing area as their planar counterparts. This study investigated finite wing aerodynamics using analytical and computational techniques. Analytical solutions using the Prandtl lifting-line equation were compared with computational solutions in OpenFOAM for rectangular, anhedral, dihedral, and circular ring wings to assess the differences between lift and drag coefficients calculated through the two methods. The analytical results only yielded reasonable results for the airfoil and rectangular wing, producing highly inaccurate values for the anhedral and dihedral wings. An analytical solution to the circular ring wing was not found due to complexity. The findings suggest that analytical methods are not feasible for evaluating nonplanar wings and that computational solvers are more effective at calculating aerodynamic properties in the majority of cases.

Keywords: Nonplanar wings, induced drag, finite wing, analytical, computational

Introduction

The first aircraft ever flown, the Wright Flyer, was also in fact the first to feature a nonplanar wing - a biplane design. Therefore, nonplanar wings technically took flight before planar wings did. While the Wright Brothers favored biplanes for their structural strength, they noticed that their wings performed better at low Reynolds numbers (Kroo, McMasters, & Smith, 1995). Multiplanes, despite being theoretically more efficient spanwise, increased parasitic drag in real life because of their construction. More promising nonplanar designs include the closed wings, which eliminate traditional wingtips and theoretically most of the wingtip vortices that form. A paper in 1995 claimed that a circular ring wing produced half the vortex drag of a rectangular wing with the same span and total lift, a sizable performance increase (Kroo, McMasters, & Smith, 1995).

Given the relatively recent interest in more advanced nonplanar wing designs, studies tend to favor using CFD software to generate solutions over analytical methods. This is also partially due to the difficulty of applying lifting-line theory to geometrically complicated shapes. This study investigates an alternative to computational solutions by making certain assumptions to make analytical methods solvable. The paper explores the extent to which these assumptions influenced the lift and drag coefficients of rectangular, anhedral, dihedral, and circular ring wings.

Methods

Thin Airfoil Theory

An analytical solution for the lift coefficient of the NACA 4412 airfoil was pursued as a benchmark. The solution was derived from the thin airfoil theory for cambered airfoils, a generalization of the symmetric airfoil (Anderson, 2011, p. 351). The thin airfoil theory was applied to the mean camber line of NACA 4412, where a transformation from cartesian to polar coordinates enabled direct integration for lift coefficient as a function of angle of attack. The integral was computed numerically for efficiency.

The Theory of Finite Wing Lift Distributions

This analysis of NACA 4412 was extended to finite wing designs using the Prandtl lifting-line equation for finite, unswept wings.

The Prandtl lifting-line theory is a mathematical model that predicts lift distribution over a three-dimensional wing based on its geometry. In this model, the vortex sheet loses strength along the whole wingspan because it is shed from the trailing edge as a whole, rather than just at the wing-tips. Over the three-dimensional wing, local lift is strongly affected by lift generated at neighbouring wing sections, and cross-sections must be analyzed with respect to other components of the airfoil.

The lifting-line theory yields the lift distribution along the span-wise direction y based on the wing geometry (span-wise distribution of the chord, airfoil, and twist) and flow conditions. In contrast to the Kutta-Joukowski theorem for two-dimensional airfoils(or any shape of infinite span), which states that $L' = -\rho_\infty V_\infty \Gamma$, in which lift distribution is the unknown variable to be calculated, the variable becomes the distribution of circulation over the span, or $\Gamma(y)$. Recall that circulation around the vortex sheet is the sum of the strengths of the elemental vortices along the chord: that is,

$$\Gamma(y) = \int_a^b \gamma ds$$

Because the vortex sheet is shed for every span-wise change in lift, the circulation changes with respect to both the span and the chord. Any span-wise change in circulation can be modelled as the shedding of a vortex filament down the flow, behind the wings. This shed vortex, whose strength is the derivative of the unknown local wing circulation distribution, $\dfrac{d\Gamma}{dy}$, influences the flow to the left and right of the wing section.

The relative differences in velocities over wing sections due to the difference in circulation over local wing sections across the span induce upwash and downwash, which is key in lifting-line theory. If the change in lift distribution is known at a given lift section, one can then predict how that section influences lift over its neighbouring sections.

2

Computational

An image of the NACA4412 airfoil was converted into a vector in Adobe Illustrator, which formed the basis of the 3D wing models in Autodesk Fusion 360. In keeping with realistic wings, the rectangular wing featured an aspect ratio of 10, similar to the de Havilland Dash 8. The rectangular wing was created by symmetrically extruding the airfoil vector along straight paths of length 1m on both sides of the axis. The anhedral and dihedral wings were created by sweeping the airfoil vector along two 5 degree-angled paths of length 1m each on both sides of the axis. Finally, the ring wing was designed by revolving the airfoil around the x-axis such that the circumference of the inner wing surface was 2m to match the other wing designs. To prevent airflow interactions with wing interiors, open wingtips were patched closed. Model rotations were made for angles of attack in increments of 5 degrees from 0-20 degrees.
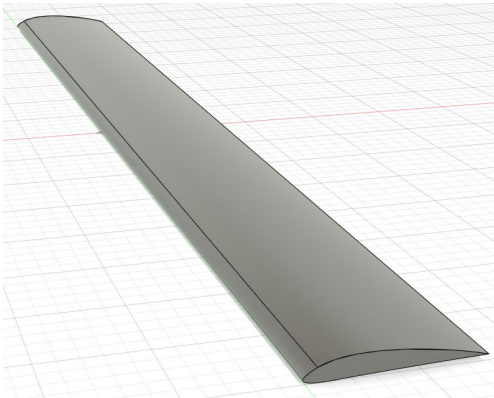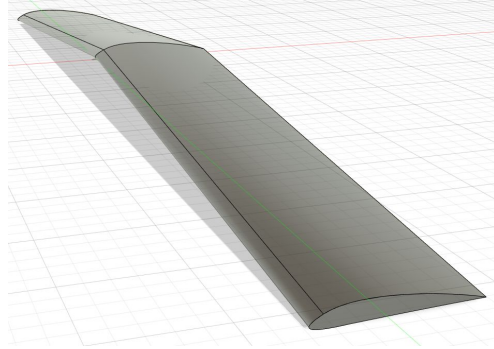

Figure 1. Rectangular wing model

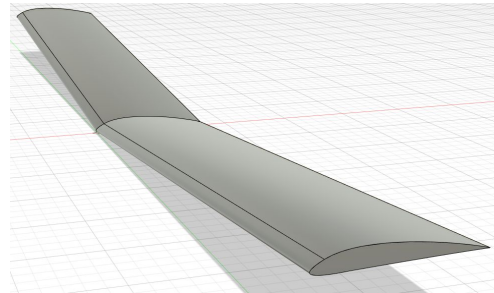*Figure 2.* Anhedral wing model
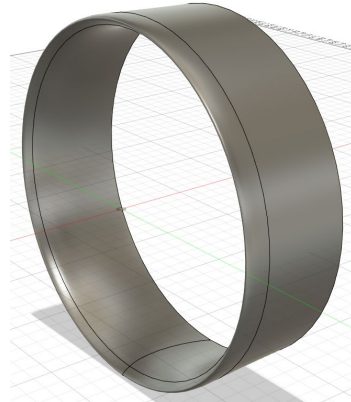

Figure 3. Dihedral wing model

Figure 4. Circular ring wing model

Next, bounding boxes (3m x 4m x 1.4m) were created for these wings, made to simulate a wind tunnel with an inlet, outlet, and four walls. The wings were placed inside these boxes such that drag was in the x direction and lift was in the z direction. The box and wing were then converted using a program called cfMesh, changing the files from .stl format, which represents the edges of 3D objects

using a set of triangles, to a format that OpenFOAM uses to run simulations. This format represents the edges of 3D objects and the volume of the bounding box using tetrahedra and polyhedra ("A Library", n.d.). These are then used as fluid elements for the simulation's calculations. A visualization of these polyhedra can be seen in Figure 5 below.
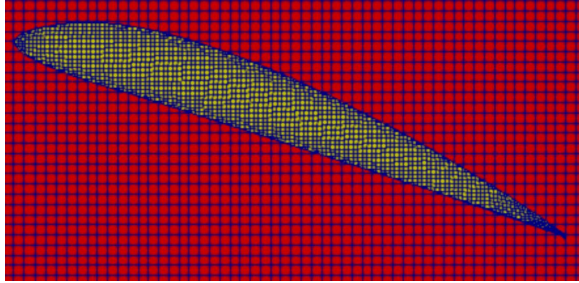

Figure 5. Rectangular wing mesh viewed from side following conversion by cfMesh

The OpenFOAM simulations used code from an airfoil tutorial modified for use with an updated OpenFOAM, 3D simulations, and custom models ("CFD support", n.d.). A solver called simpleFoam was used. This is a steady state solver, which attempts to converge to a state of time independent fluid flow (as opposed to a transient solver, which assumes time dependent fluid flow). The steady state solver greatly reduced computational cost and runtime of the simulations.

With simpleFoam, a timestep of one second was used and the flow was simulated for 1500 seconds, resulting in runtimes of less than 2.5 hours on eight CPU core virtual machines, which allow eight computational processes to be run simultaneously. This is in contrast to transient solvers such as pimpleFoam, which require much smaller time steps. This is because transient solvers require that the

Courant number never be greater than one, with a similar condition applied to the y and z axes.

$$C \equiv \frac{u \Delta t}{\Delta x} \leq 1$$

The relation is shown in the above equation, where u is the velocity of the fluid in the x direction, Δt is the timestep, and Δx is the length of the fluid element (Giraldo, n.d.). This condition ensures that the fluid flow never moves farther than the length of a fluid element in a single time step and, with the high velocity flows used in our simulations, this resulted in timesteps as small as $3*10^{-5}$ s. Since the fluid flow was simulated for around a second, this led to runtimes of longer than 6 hours, even on 32 CPU core virtual machines. For these reasons, transient solvers were infeasible.

The simulations assumed the wings travelled at 90 m/s and that the fluid was incompressible. Kinematic viscosity ($v = \mu / \rho$ where v = kinematic viscosity, μ = absolute or dynamic viscosity, and ρ = density) was set to $3*10^{-5}$ ("Absolute, Dynamics," 2003).This led to a Reynolds number of approximately 600,000. The reference area used to calculate lift coefficients was constant throughout simulations as 0.4 m^2, calculated by multiplying the wing and chord lengths.

The code used to run simulations can be found on GitHub at: https://github.com/jhargun/OpenFoam-Example. The difference between this example and the code used to simulate wings is the constant/polyMesh folder, which normally contains the mesh that represents the wing but was removed from the example due to Github's file size limitation.
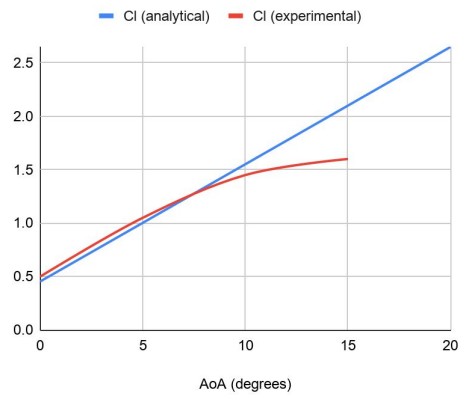
Results

Figure 6. Analytical and experimental lift coefficients for NACA4412 airfoil at various angles of attack using mean camber line and thin airfoil theory.
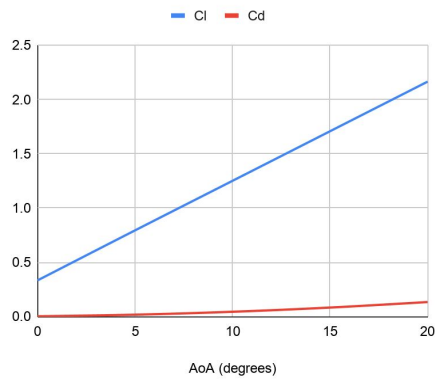

Figure 7. Lift and drag coefficients for NACA4412 airfoil at various angles of attack assuming elliptical lift distribution.
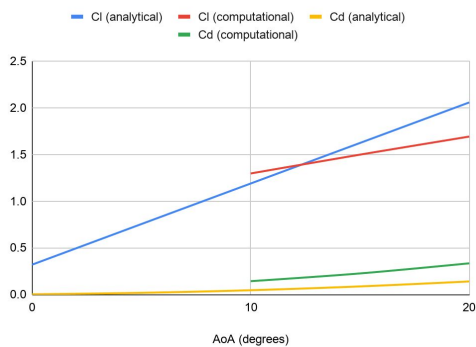

Figure 8. Analytical and computational lift and drag coefficients for NACA4412 rectangular wing at various angles of attack.
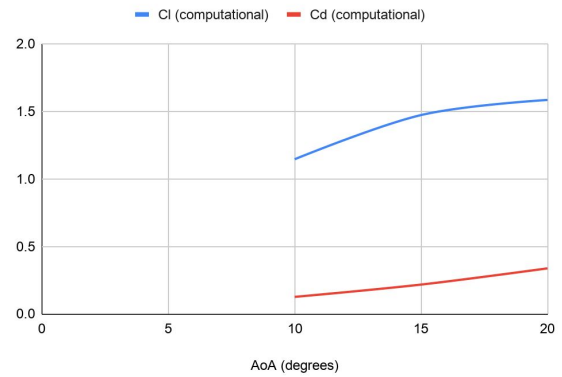

Figure 9. Analytical and computational lift and drag coefficients for NACA4412 anhedral wing at various angles of attack.
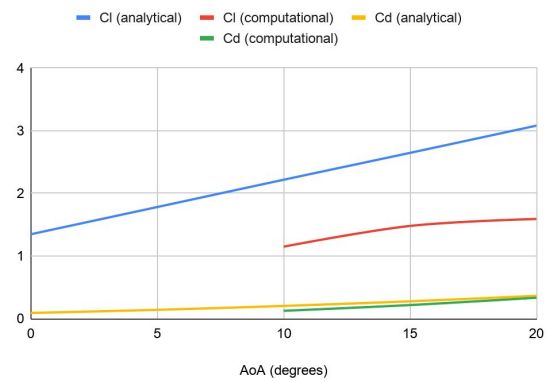

Figure 10. Analytical and computational lift and drag coefficients for NACA4412 dihedral wing at various angles of attack.
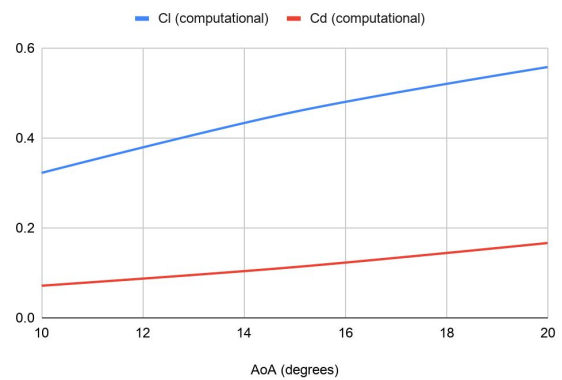

Figure 11. Analytical and computational lift and drag coefficients for NACA4412 circular ring wing at various angles of attack.

The analytical results for the airfoil from thin airfoil theory agreed with data from web sources for angles of attack below 15 degrees, from which the results began to differ ("NACA4412", n.d.). Once an elliptical lift distribution for finite wings is assumed, the lift coefficient decreased slightly by about 26%.

Due to time and cost constraints, computer simulations were not run for 0 and 5 degree angles of attack. For the rectangular wing, the analytical and computational solutions had minimal deviations. The computational solutions produced larger lift and drag coefficients. Given more time to complete the remaining simulations, it is reasonable to expect values that agree with the analytical solution.

For the nonplanar wings, the analytical solutions produce lift and drag coefficients wildly different from those of the computational solutions. There was some discrepancy between the analytical and computational results in the dihedral wing. The analytical solution returned lift coefficients nearly double those given by computational solving. Most bizarrely, the analytical solution gives *negative* lift coefficients for angles of attack of 0 and 5 degrees for the anhedral wing. On the other hand, the drag coefficients from both methods were similar at angles of attack of 15 and 20 degrees.

While theoretically possible, an analytical solution for the circular ring wing was not pursued due to time and difficulty. Therefore, the computational results shall serve as a "proof-of-concept". The circular ring wing performed terribly under simulated conditions, with high angle of attack lift coefficients comparable to low angle of attack lift coefficients of the rectangular wing albeit with marginally higher drag coefficients.

The computational solving process produced further information on the aerodynamic characteristics of the wings. The velocity and pressure distributions are located in the *Supplement* section of this report. Tables containing information about calculated forces and coefficients are also included in this section.

Discussion

In the basic comparison between experimental data and analytical solutions for the NACA4412 airfoil using thin airfoil theory, there was little difference between lift coefficients from 0 to 10 degree angles of attack. However, the gap widened at a 15 degree angle of attack. Since thin airfoil theory ignores viscous effects, it is likely that at high angles of attack, viscous effects significantly affect the airflow stability and thus the lift coefficient. This conclusion is supported by computational results. For every wing shape, the size of the wake left behind by instability resulting from viscous forces increased as angle of attack increased. One should note that the lifting-line theory for finite wings similarly does not take into account viscous forces, and thus, this must be considered when comparing the analytical and computational discrepancies.

The reasons behind the massive difference between analytical and computational results for the anhedral and dihedral wing are unclear. Evidence suggests that, at *supersonic* speeds, dihedral wings generally have slightly lower lift coefficients compared to rectangular wings (Powell, 1956). Since the angled component of the dihedral causes horizontal lift production (which provides lateral roll stability), it is fair to assume that this effect applies to subsonic flow as well. This logic can be extended to the anhedral wing. However, it does not explain the negative lift coefficients from the analytical solution. Negative values imply a downwards lift force, which appears to be a physical contradiction since the airfoil fulfills the Kutta condition. Most likely, the computational

solutions are correct and the analytical solutions are incorrect.

A possible reason for this analytical discrepancy could be the application of geometric twist in calculating the dihedral/anhedral of the wing. None of the consulted sources mentioned modifications needed to analyze dihedral/anhedral wings, so their dihedral property was equated to a wash-in from geometric twist. This equivalence, in retrospect, may have been wrong.

It is also worth noting the evolution of the Oswald efficiency factor in the calculations of dihedral and anhedral. The Oswald efficiency factor accounts for induced drag and is equal to 1 for elliptical lift distributions. Indeed, when analytically calculating the coefficients of drag for the rectangular wing, the efficiency factor was about 0.956, no matter the angle of attack - an unsurprising result given the proximity in value between the elliptical approximation calculations and the Prandtl calculations for the rectangular wing. Conversely, analysis of dihedral and anhedral drag yields efficiency factors that average to about 0.7 and 0.4 respectively, although the anhedral's efficiency factors fluctuated significantly with respect to those of the dihedral.

As always, such analytical computations are subject to human error. One way to increase the accuracy of the results would be to increase the number of control points N. While the plane of symmetry was used to simplify the equations (knowing that the chosen y-coordinates on the port wing would have the same magnitude as the y-coordinates on the starboard wing), introducing more y-coordinates would have yielded more accurate results for the Fourier amplitudes but also a significantly more complicated series.

Upon inspection of the computational data, the velocity and pressure distributions for rectangular, anhedral, and dihedral wings highlight the effect of

turbulence and edge effects, with vortices clearly visible when looking at the y directional velocity distributions (as shown in Figure 12). Notably, the ring wing lacks these vortices as it lacks clearly defined edges.
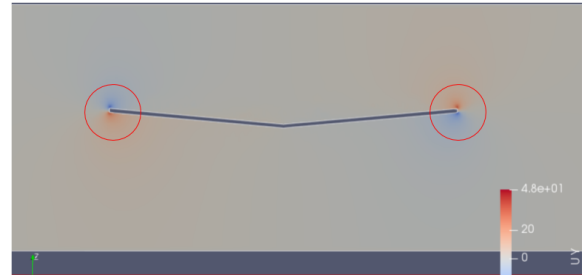

Figure 12. Velocity distribution in y direction for dihedral wing with 10 degree angle of attack (viewed from front) with evidence of vortices circled.
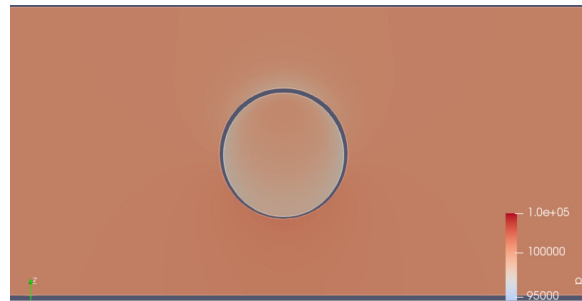

Figure 13. Pressure distribution (in Pascals) for ring wing with 10 degree angle of attack (viewed from front).

There are numerous explanations for the ring wing's poor aerodynamic performance. As shown above in Figure 13, the ring wing lacks a well-defined pressure difference. Rectangular, dihedral, and anhedral wings have higher pressure below the wing than above, meaning the pressure force contributes to lift. Without this pressure difference, the ring wing does not benefit from this source of lift. Moreover, a large portion of the wing area is aligned vertically, contributing little *upward* lift force. Instead, the forces on the body negate each other. This effect is visible in Table 10. This presents structural problems for real-world applications, where additional reinforcement to resist the effects of the forces on the

vertical portions of the wing would add weight for no aerodynamic improvement. While the viscous force (or lack thereof) adds less drag and takes away less lift, this change is small compared to the massive reduction in pressure forces, leading to a much smaller lift.

Even the computational results were not perfect. Some decisions were made to reduce simulation runtimes, possibly increasing the margin of error. For example, the flow was assumed incompressible and a faster turbulence model was used. The model, RANS, can achieve faster runtimes than the alternative model, LES, but fails to model small eddies. These assumptions certainly contributed to the final results. Regardless, the computational models were still able to get closer to experimental results because they made relatively fewer assumptions than the analytical method.

Conclusion

The results confirmed underlying suspicions that the computational values would be more accurate than the analytical ones. Initially, the project began with expectations that solving analytically for lift and drag coefficients of nonplanar wings would be tricky, but should yield reasonable values. In the case of the ring wing, a solution was attempted but not completed due to its sheer difficulty.

As the assumptions made by analytical solutions grew, so did the argument in favor of computational solving. As shown in the anhedral and dihedral wings, the analytical solution produced values that deviated far from expected results. Negative lift coefficients in the anhedral wing analysis suggest critical flaws in the calculation process likely stemming from use of geometric twist to account for the angle. The evidence strongly suggests that CFD programs are more effective for testing aerodynamic characteristics, being able to examine wings more accurately than analytical methods that rely on ideal conditions to simplify problems. While it should be possible to find better ways to analyze nonplanar wings without computers, the effort is better directed towards improving numerical methods instead, in creating more realistic turbulent flow models and optimizing code for faster runtime and greater precision.

The results suggest that attempting to examine nonplanar wing shapes using traditional analytical methods is not only cumbersome and complicated, but also inaccurate. The benefits of using analytical methods for shapes beyond simple rectangular wings are unclear. Provided the code functions correctly, the benefits of computational solving far outweigh the relatively small margins of error.

Acknowledgements

References

Absolute, Dynamics, and Kinematic Viscosity. (2003). Retrieved from

https://www.engineeringtoolbox.com/dynamic-absolute-kinematic-viscosity-d_412.html

Airfoil in OpenFOAM. (n.d.). Retrieved from http://hmf.enseeiht.fr/travaux/projnum/book/export/html/3151

Anderson, J. D. (2011). *Fundamentals of aerodynamics* (5th ed.). New York: McGraw-Hill.

ANSYS Fluent. (n.d.). Retrieved February 12, 2020, from ANSYS website:

http://ansys.com/products/fluids/ansys-fluent

Auld, D. J., & Srinivas, K. (n.d.). 3D Prandtl Lifting Line Theory. In *Aerodynamics for Students*. Retrieved

June 3, 2020, from

http://www.aerodynamics4students.com/subsonic-aerofoil-and-wing-theory/3d-prandtl-lifting-line-t

heory.php

Cantwell, B. (n.d.). Chapter 12: Wings of Finite Span. In *AA200_Course_Material* (pp. 1-61). Retrieved

June 3, 2020, from

https://web.stanford.edu/~cantwell/AA200_Course_Material/AA200_Course_Notes/AA200_Ch_1

2_Wings_of_Finite_Span_Cantwell.pdf

CFD support. (n.d.). Retrieved from https://www.cfdsupport.com/download-cases-NACA4412.html

Depshande, M. D., Prof. (n.d.). *Finite Wing Theory* [pdf]. Retrieved from

http://164.100.133.129:81/econtent/Uploads/ACD2505-09-%20Finite%20Wing%20Theory.pdf

Giraldo, F. X. (n.d.). *Time-Integrators*. Retrieved from

http://faculty.nps.edu/fxgirald/projects/nseam/nps/new_section4.pdf

Greenshields, C. (2017, March 2). OpenFoam User Guide. Retrieved from

https://cfd.direct/openfoam/user-guide/

Gschaider, B. (2019, July 27). Unofficial OpenFOAM wiki. Retrieved January 31, 2020, from

OpenFOAMWiki website: http://openfoamwiki.net/index.php/Main_Page

Hart, T. (2014, November 19). Re: PDF User Manual for Fusion 360 [Ultimate] [Online forum post].

Retrieved from

https://forums.autodesk.com/t5/fusion-360-design-validate/pdf-user-manual-for-fusion-360-ultimat

e/m-p/5416329#M57786

Jackson, D. (2001, December 2). Wing Twist and Dihedral [Online forum post]. Retrieved from

http://www.aerospaceweb.org/question/dynamics/q0055.shtml

Kroo, I., McMasters, J., & Smith, S. C. (1995, September 26). *Highly Nonplanar Lifting Systems*. Retrieved

from https://ntrs.nasa.gov/archive/nasa/casi.ntrs.nasa.gov/19960023622.pdf

Kroo, I. M. (2005, June). *Nonplanar wing concepts for increased aircraft efficiency* [Speech transcript].

Retrieved January 31, 2020, from LF5422 Micheville website:

https://lf5422.com/wp-content/uploads/2014/08/vki_nonplanar_kroo-1.pdf

A Library for Automatic Mesh Generation [cfMesh]. (n.d.). Retrieved from https://cfmesh.com/cfmesh/

NACA 4412 (naca4412-il). (n.d.). Retrieved from http://airfoiltools.com/airfoil/details?airfoil=naca4412-il

OpenFOAM on Google Compute Engine. (n.d.). Retrieved from

http://www.variousconsequences.com/2012/10/openfoam-on-google-compute-engine.html

Powell, J. B. L. (1956). The Effect Of Dihedral On The Lift And Drag Coefficients Of Airfoils In Supersonic

Flow. *The Quarterly Journal of Mechanics and Applied Mathematics*, *9*(1), 52–74. doi:

10.1093/qjmam/9.1.52

SimScale Documentation. (2019, April 29). Retrieved February 12, 2020, from SimScale website:

https://www.simscale.com/docs/

White, F. M. (2011). *Fluid Mechanics* (7th ed.). New York, NY: McGraw-Hill.

Winarto, H. (2004, May). *Lifting Line Theory* [pdf]. Retrieved from

https://ftp.unpad.ac.id/orari/library/library-non-ict/aero/docs/LIFTING%20LINE%20THEORY%20T

utorial%20Example.pdf

Supplement

Table of values for lift and drag coefficient plots

Table 1. Comparison of analytical and experimental (web) solutions for lift coefficients of NACA4412 airfoil

AoA	Cl (analytical)	Cl (experimental)
0	0.4544	0.5
5	1.0027	1.05
10	1.5510	1.45
15	2.0993	1.6
20	2.6477	

Table 2. Elliptical lift distribution approximations for lift and drag coefficients for NACA 4412 airfoil

AoA	Cl	Cd
0	0.334	0.003268463
5	0.7950533	0.018140427
10	1.2519	0.04498296
15	1.708904	0.0838089
20	2.16583	0.134618148

Table 3. Comparison of analytical and computational solutions for lift and drag coefficients for NACA 4412 rectangular wing.

AoA	Cl (analytical)	Cl (computational)	Cd (analytical)	Cd (computational)
0	0.32044		0.00341665	
5	0.75491611		0.018963021	
10	1.188773	1.2962886	0.04702	0.14368372
15	1.62263203879	1.4976872	0.0876093151662	0.22650101
20	2.05649066	1.691214	0.140722545	0.3348565

Table 4. Comparison of analytical and computational solutions for lift and drag coefficients for NACA 4412 anhedral wing.

AoA	Cl (analytical)	Cl (computational)	Cd (analytical)	Cd (computational)
0	-0.70307		0.0424602	
5	-0.2691569		0.0239091	
10	0.164704	1.1468558	0.0178925	0.12705124
15	0.59856	1.4743812	0.02440314	0.21828773
20	1.01430	1.5862835	0.0422595	0.33849831

Table 5. Comparison of analytical and computational solutions for lift and drag coefficients for NACA 4412 dihedral wing.

AoA	Cl (analytical)	Cl (computational)	Cd (analytical)	Cd (computational)
0	1.3485126		0.09288450	
5	1.782400779		0.14333865	
10	2.2176995	1.1506751	0.205691	0.12761324
15	2.64653785	1.4812911	0.279264103	0.21964621
20	3.0805629	1.5925439	0.36648466	0.33619325

Table 6. Computational lift and drag coefficients for NACA 4412 circular ring wing.

AoA	Cl	Cd
10	0.32250077	0.071228805
15	0.45846843	0.1126985
20	0.55811035	0.16628217

Table 7. Lift and drag forces (measured in Newtons) calculated computationally for rectangular wings.

AoA	Lift from Pressure	Drag from Pressure	Lift from Viscous Force	Drag from Viscous Force
10	2529.1063	259.7498	-2.8212455	20.269646
15	2922.2019	424.16323	-3.4190917	17.255529
20	3299.217	639.20968	-3.2776687	13.378759

Table 8. Lift and drag forces (measured in Newtons) calculated computationally for anhedral wings.

AoA	Lift from Pressure	Drag from Pressure	Lift from Viscous Force	Drag from Viscous Force
10	2237.8715	227.46094	-2.8100267	20.14415
15	2876.844	408.01951	-3.4815442	17.392714
20	3094.7584	646.61694	-3.3138765	13.068877

Table 9. Lift and drag forces (measured in Newtons) calculated computationally for dihedral wings.

AoA	Lift from Pressure	Drag from Pressure	Lift from Viscous Force	Drag from Viscous Force
10	2245.3182	228.43172	-2.8135002	20.268614
15	2890.3297	410.45834	-3.5007513	17.601374
20	3106.9205	641.91682	-3.2753797	13.276746

Table 10. Lift and drag forces (measured in Newtons) calculated computationally for ring wings.

AoA	Lift from Pressure	Drag from Pressure	Lift from Viscous Force	Drag from Viscous Force
10	629.89945	119.32372	-1.3905951	19.49125
15	895.23698	201.43155	-1.7461918	18.202053
20	1089.6941	306.82239	-2.0151289	17.238274

Lift coefficient of NACA4412 airfoil from mean camber line

$$\frac{z}{c} = \begin{cases} 0.25 \left[0.8\frac{x}{c} - \left(\frac{x}{c}\right)^2 \right] & 0 \leq \frac{x}{c} \leq 0.4 \\ 0.111 \left[0.2 + 0.8\frac{x}{c} - \left(\frac{x}{c}\right)^2 \right] & 0.4 \leq \frac{x}{c} \leq 1 \end{cases}$$

$$\frac{dz}{dx} = \begin{cases} 0.25 \left[0.8 - \frac{2x}{c} \right] & 0 \leq \frac{x}{c} \leq 0.4 \\ 0.111 \left[0.8 - \frac{2x}{c} \right] & 0.4 \leq \frac{x}{c} \leq 1 \end{cases}$$

$$\text{transform} \quad x = \frac{c}{2}(1 - \cos(\theta))$$

$$\frac{dz}{dx} = \begin{cases} 0.25 \left(-0.2 + \cos\theta \right) & 0 \leq \theta \leq 1.369 \\ 0.111 \left(-0.2 + \cos\theta \right) & 1.369 \leq \theta \leq \pi \end{cases}$$

$$C_l = 2\pi \left[\alpha + \frac{1}{\pi} \left(\int_0^{1.369} 0.25(-0.2 + \cos\theta)(\cos\theta - 1)d\theta + \int_{1.369}^{\pi} 0.111(-0.2 + \cos\theta)(\cos\theta - 1)d\theta \right) \right]$$

$$C_l = 2\pi\alpha + 0.4544$$

Calculating Coefficients of Lift and Drag using Lifting-Line Theory

The unknown vortex strength distribution can be modelled as follows, approximated by a Fourier Series:

$$\Gamma(\theta) = 2bV \sum_{n=1}^{N} A_n \sin(n\theta)$$

(1)

The basic problem then, is how to calculate the unknown Fourier series for amplitudes A_n

$$y = -\frac{b}{2} \cos\theta$$

(2)

The variable y indicates the points along the span b as measured from the wing root (the root of the airfoil is the airfoil located at the plane of symmetry- the center- if one were to connect the two wings without the fuselage).

We can express θ as follows:

$$\theta = \cos^{-1}\left(-\frac{2y}{b}\right)$$

(3)

The approximation of the aforementioned Fourier series becomes more accurate as we increase the number of terms N. However, for the sake of simplicity (and due to the fact that these values were calculated analytically by hand), we opted to use 4 terms, as more terms correspond to increasingly complex equations.

The lifting line equation that needs to be solved is:

$$\frac{4b}{a(y)c(y)} \sum_{n=1}^{N} A_n \sin(n\theta(y)) + \sum_{n=1}^{N} nA_n \frac{\sin(n\theta(y))}{\sin(\theta(y))} = \alpha_G(y) - \alpha_0(y)$$

(4)

b is the span

$c(y)$ is the spanwise chord length

$\alpha_G(y)$ is the geometric angle of incidence

$\alpha_0(y)$ is the zero lift angle of incidence

$a(y)$ is the section lift slope

Zero Lift Angle of Incidence

The zero lift line is the line through the airfoil along which relative airflow produces no lift. A cambered airfoil generates no lift when it is moving parallel to the zero-lift axis, which is dependent on the camber of the airfoil. The zero lift angle for any cambered airfoil can be calculated as follows:

$$\text{Zero-lift angle (radians)} = \tan^{-1}(m/1-p)) \quad \text{(5)}$$

M is the camber (the maximum height between the camber line and the chord line), and p is the horizontal displacement of the camber.

The lifting line equation can be simplified:

$$\sum_{n=1}^{N} \left(\left(\frac{4b}{a(y)c(y)} + \frac{n}{sin(\theta(y))} \right) \sin(n\theta(y)) \right) A_n = \alpha_G(y) - \alpha_0(y) \quad \text{(6)}$$

Let us express the left side of the equation as a function of C, where:

$$C(y,n) = \left(\frac{4b}{a(y)c(y)} + \frac{n}{\sin(\theta(y))} \right) \sin(n\theta(y)) \quad \text{(7)}$$

And let us express the right side of the equation as a function of D, where:

$$D(y) = \alpha_G(y) - \alpha_0(y) \quad \text{(8)}$$

$$\sum_{n=1}^{N} C(y,n)A(n) = D(y) \quad \text{(9)}$$

$$A(n) = A_n \quad \text{(10)}$$

This simplified equation should be applied to N different control points, so that we have a system of equations that can be solved simultaneously to calculate the values of A(n). N points along the span are chosen so that they are evenly spaced: the span is divided into N equal intervals, and the midpoint of each interval is chosen to be a control point. N should be an even integer, such that N = 2M, where M is an arbitrary natural number.

The coordinates of the control points can be calculated as follows:

$$y(k) = y_k = -\frac{b}{2}\left(1 - \frac{2k-1}{N}\right) \quad 1 \le k \le N$$

(9)

Note that the control points are symmetric about the plane of symmetry.

It can be shown that the Fourier terms with even indices are equal to zero, such that:

$$A_{2m} = 0$$ (10)

$$1 \le m \le M \quad (M = 0.5N)$$

Equation 1 can then be simplified as follows:

$$\Gamma(\theta) = \sum_{n=1}^{N} A_n \sin(n\theta) = 2bV\left[\sum_{n=1}^{M} A_n \sin((2m-1)\theta) + \sum_{n=1}^{M} A_n \sin(2m\theta)\right]$$

(11)

$$\Gamma(\theta) = 2bV\sum_{n=1}^{M} A_{2m-1} \sin((2m-1)\theta) = 2bV\sum_{n=1}^{M} A(2m-1) \sin((2m-1)\theta)$$

(12)

The system of equations that needs to be solved, therefore, can be expressed as follows, substituting the corresponding values of k and m for variables y and n, respectively:

$$\sum_{m=1}^{M} C(k, 2m-1)A(2m-1) = D(k)$$

(13)

$$\theta_k = \theta(k) = \theta(y_k) = \cos^{-1}\left(1 - \frac{2k-1}{2M}\right)$$

$$C(k, 2m-1) = C(\theta_k, 2m-1) = \left(\frac{4b}{a(k)c(k)} + \frac{2m-1}{\sin(\theta_k)}\right)\sin((2m-1)\theta_k)$$

$$D(k) = \alpha_G(k) - \alpha_0(k) = \alpha_G(y_k) - \alpha_0(y_k)$$

After selecting the value of N (in all of our calculations, N = 4 was used), one solves for the desired value of A_1 most efficiently using by forming an augmented coefficient matrix using the corresponding values of C, A, and D, and solving for A by using Gaussian elimination.

Once one has solved for A(1), one can solve for the coefficient of lift using:

$$C_L = \pi A R A_1$$

The coefficient of drag can then be calculated using:

$$C_{Di} = \frac{C_L^2}{\pi A R e},$$

e, also known as the Oswald efficiency factor, can be calculated as follows:

$$e = \frac{1}{1 + \delta}$$

$$\delta = \frac{\sum_{n=2}^{\infty} n A_n^2}{A_1^2}$$

Elliptical Lift Distribution Approximation

This approximation causes the downwash across the span to be constant due to the almost uniform lift distribution. With this approximation, the equations of the coefficient of lift and drag are as follows:

$$C_L = C_{l\alpha} \left(\frac{AR}{AR + 2} \right) \alpha$$

$C_{l,\alpha}$ is the two-dimensional coefficient slope and AR is the aspect ratio, span over chord.

$$C_{Dinduced} = \frac{C_L^2}{\pi A R}$$

Calculations for Dihedral and Anhedral

Wings with geometric twist are wings in which there is a height difference between the leading edge of the root airfoil and the leading edge of the wingtips, such that the geometric angle of attack varies across the span. In contrast, a wing without twist (such as the rectangular NACA 4412 wing) is one where the geometric angle of attack is constant for all y-values.

A washout (anhedral) is when the wing is twisted such that the leading edge of the root is higher than the leading edge of the wingtip. A washin(dihedral) is when the wing is twisted such that the leading edge of the root is lower than the leading edge of the wingtip.

Geometric twist modifies the equation of the angles as follows:

$$\alpha_G(k) = \alpha + \beta(k)$$
$$D(k) = \alpha - \alpha_0(k) + \beta(k)$$

Where β(k) can be expressed as:

$$\beta(k) = \sin\left(-\frac{2y}{bc}h_{tip}\right) = \sin^{-1}\left(\left(1 - \frac{2k-1}{N}\right)\frac{h_{tip}}{c}\right)$$

Washout corresponds to negative values of **h**, while washin corresponds to positive values of **h**.

Rectangular Wings
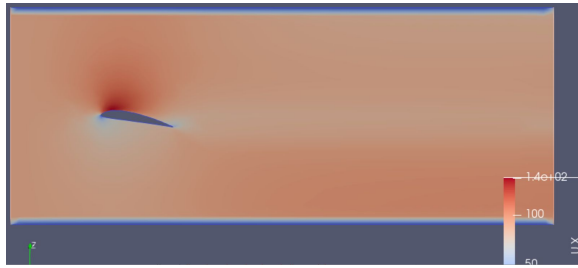
Figure 14. Velocity distribution in x direction for rectangular wing with 10 degree angle of attack (viewed from side)
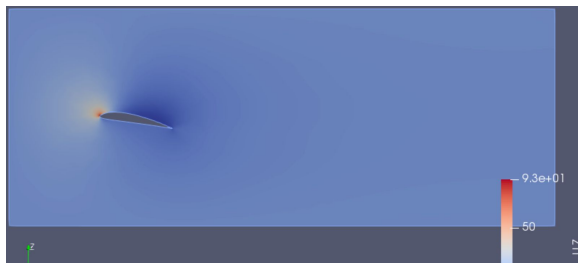
Figure 15. Velocity distribution in z direction for rectangular wing with 10 degree angle of attack (viewed from side)
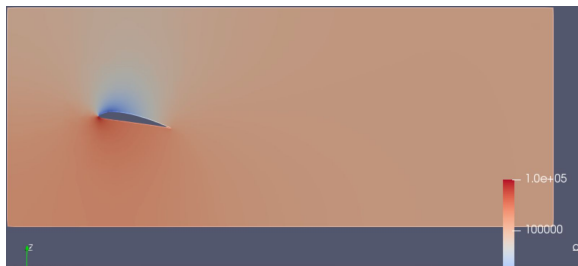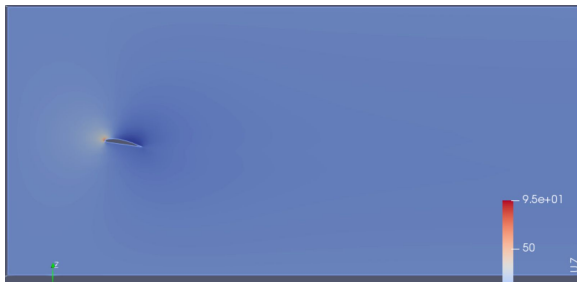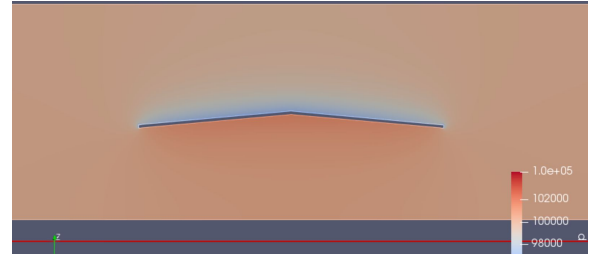

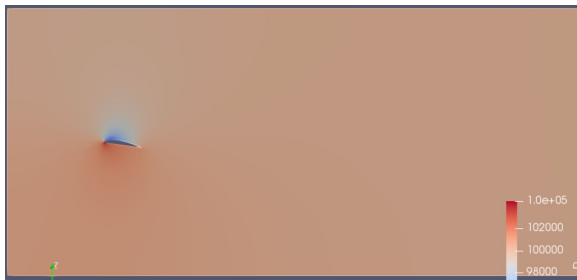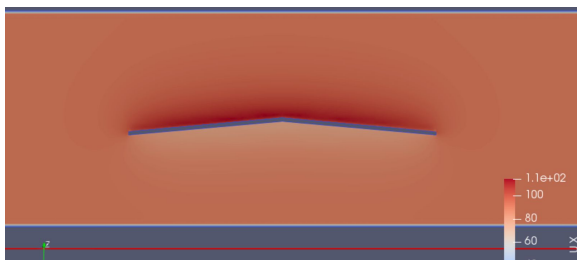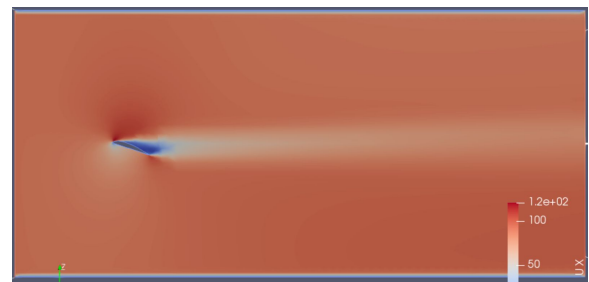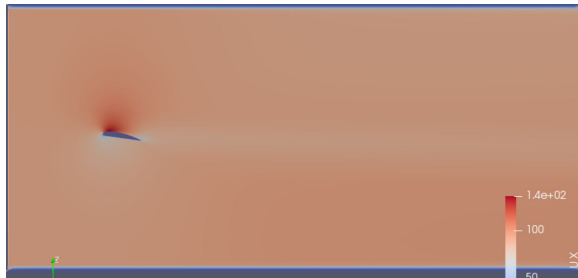*Figure 16.* Pressure distribution (in Pascals) for rectangular wing with 10 degree angle of attack (viewed from side)
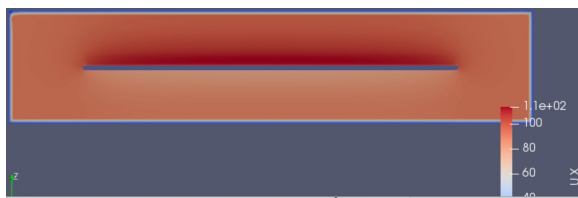
Figure 17. Velocity distribution in x direction for rectangular wing with 10 degree angle of attack (viewed from front)
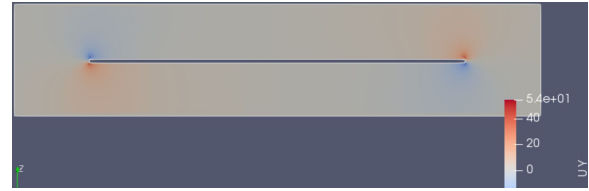
Figure 18. Velocity distribution in y direction for rectangular wing with 10 degree angle of attack (viewed from front)

Figure 19. Velocity distribution in x direction for rectangular wing with 15 degree angle of attack (viewed from side)

Figure 20. Velocity distribution in x direction for rectangular wing with 20 degree angle of attack (viewed from side)

Anhedral Wings (side photos taken at center of wing)
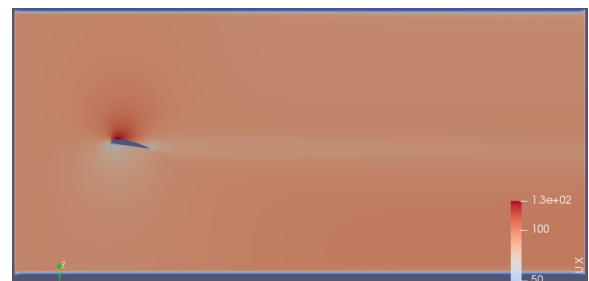
Figure 21. Velocity distribution in x direction for anhedral wing with 10 degree angle of attack (viewed from side)
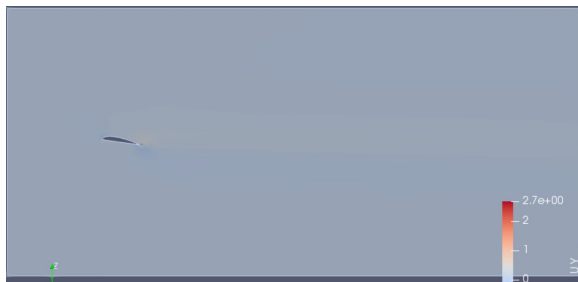
Figure 22. Velocity distribution in y direction for anhedral wing with 10 degree angle of attack (viewed from side)
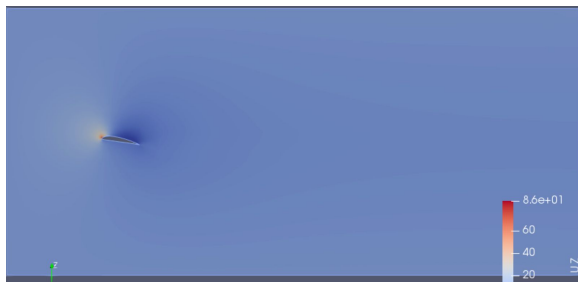

Figure 23. Velocity distribution in z direction for anhedral wing with 10 degree angle of attack (viewed from side)

Figure 24. Pressure distribution (in Pascals) for anhedral wing with 10 degree angle of attack (viewed from side)
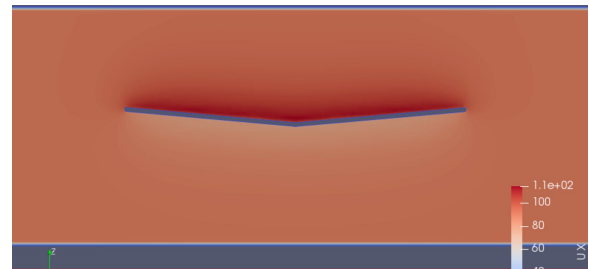

Figure 25. Velocity distribution in x direction for anhedral wing with 10 degree angle of attack (viewed from front)
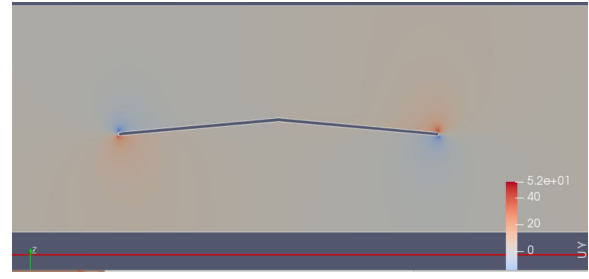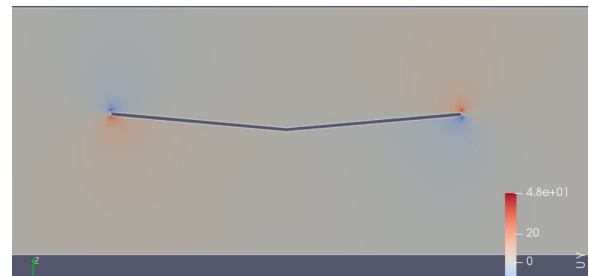

Figure 26. Velocity distribution in y direction for anhedral wing with 10 degree angle of attack (viewed from front)
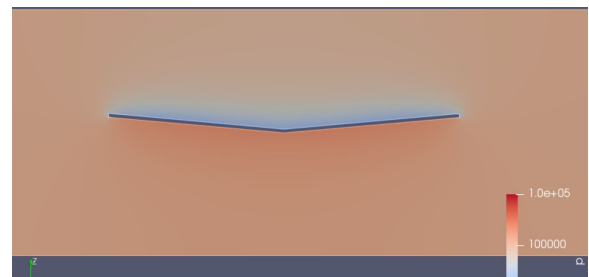

Figure 27. Pressure distribution (in Pascals) for anhedral wing with 10 degree angle of attack (viewed from front)

Figure 28. Velocity distribution in x direction for anhedral wing with 15 degree angle of attack (viewed from side)

Figure 29. Velocity distribution in x direction for anhedral wing with 20 degree angle of attack (viewed from side)

Dihedral Wings (side photos taken at center of wing)

Figure 30. Velocity distribution in x direction for dihedral wing with 10 degree angle of attack (viewed from side)

Figure 31. Velocity distribution in y direction for dihedral wing with 10 degree angle of attack (viewed from side)

Figure 32. Velocity distribution in z direction for dihedral wing with 10 degree angle of attack (viewed from side)

Figure 33. Pressure distribution (in Pascals) for dihedral wing with 10 degree angle of attack (viewed from side)

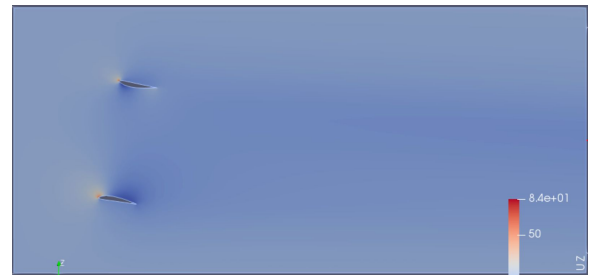*Figure 34.* Velocity distribution in x direction for dihedral wing with 10 degree angle of attack (viewed from front)

Figure 35. Velocity distribution in y direction for dihedral wing with 10 degree angle of attack (viewed from front)

Figure 36. Pressure distribution (in Pascals) for dihedral wing with 10 degree angle of attack (viewed from front)

Figure 37. Velocity distribution in x direction for dihedral wing with 15 degree angle of attack (viewed from side)

Figure 38. Velocity distribution in x direction for dihedral wing with 20 degree angle of attack (viewed from side)

Ring Wings (side photos taken at center of wing)

Figure 39. Velocity distribution in x direction for ring wing with 10 degree angle of attack (viewed from side)
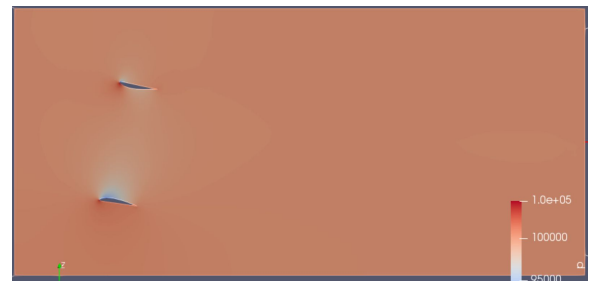

Figure 40. Velocity distribution in y direction for ring wing with 10 degree angle of attack (viewed from side)

Figure 41. Velocity distribution in z direction for ring wing with 10 degree angle of attack (viewed from side)

Figure 42. Pressure distribution (in Pascals) for ring wing with 10 degree angle of attack (viewed from side)
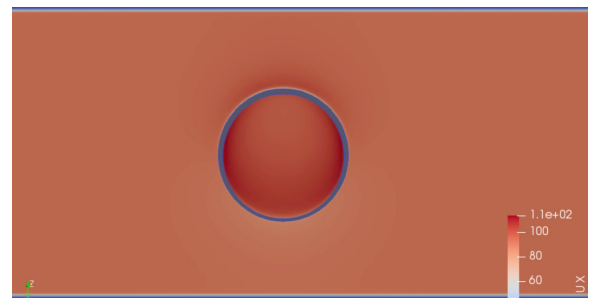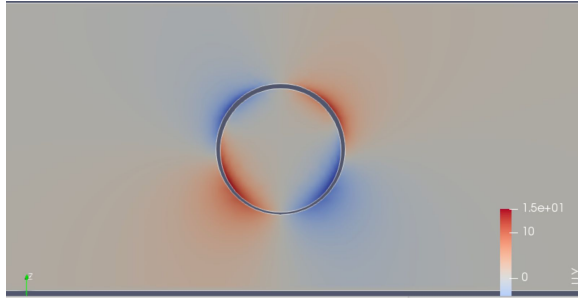

Figure 43. Velocity distribution in x direction for ring wing with 10 degree angle of attack (viewed from front)

Figure 44. Velocity distribution in y direction for ring wing with 10 degree angle of attack (viewed from front)
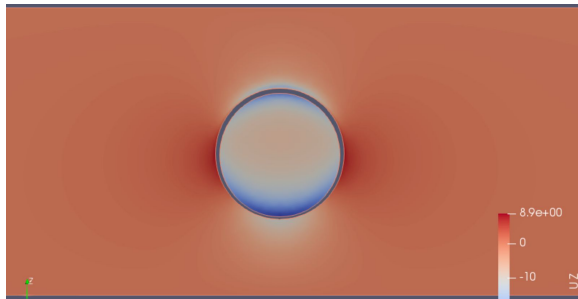

Figure 45. Velocity distribution in z direction for ring wing with 10 degree angle of attack (viewed from front)
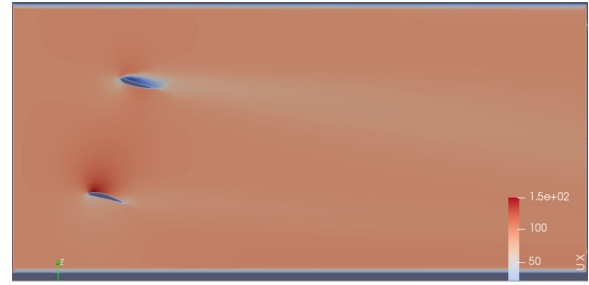

Figure 46. Velocity distribution in x direction for ring wing with 15 degree angle of attack (viewed from side)
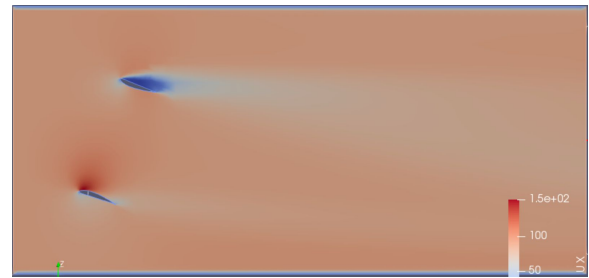

Figure 47. Velocity distribution in x direction for ring wing with 20 degree angle of attack (viewed from side)